remote sensing

MDPI

Article

Observed Retrogressive Thaw Slump Evolution in the Qilian Mountains

Xingyun Liu [1], Xiaoqing Peng [1,2,*], Yongyan Zhang [3], Oliver W. Frauenfeld [4], Gang Wei [1], Guanqun Chen [1], Yuan Huang [1], Cuicui Mu [1,2] and Jun Du [5]

[1] Key Laboratory of Western China's Environmental Systems (Ministry of Education), College of Earth and Environmental Sciences, Lanzhou University, Lanzhou 730000, China; liuxingyun21@lzu.edu.cn (X.L.); weig2023@lzu.edu.cn (G.W.); chengq2023@lzu.edu.cn (G.C.); hyuan2023@lzu.edu.cn (Y.H.); mucc@lzu.edu.cn (C.M.)
[2] Observation and Research Station on Eco-Environment of Frozen Ground in the Qilian Mountains, Lanzhou University, Lanzhou 730000, China
[3] Qinghai Provincial General Geological and Environmental Monitoring Station (Qinghai Provincial Geological Disaster Prevention and Control Technical Guidance Center), Xining 810000, China; zyyzl20150531@163.com
[4] Department of Geography, Texas A&M University, College Station, TX 77843, USA; oliver.frauenfeld@tamu.edu
[5] Key Laboratory of Ecological Safety and Sustainable Development in Arid Lands, Northwest Institute of Eco-Environment and Resources, Chinese Academy of Sciences, Lanzhou 730000, China; dujun2012@lzb.ac.cn
* Correspondence: pengxq@lzu.edu.cn

Abstract: Climate warming can lead to permafrost degradation, potentially resulting in slope failures such as retrogressive thaw slumps (RTSs). The formation of and changes in RTSs could exacerbate the degradation of permafrost and the environment in general. The mechanisms of RTS progression and the potential consequences on the analogous freeze–thaw cycle are not well understood, owing partly to necessitating field work under harsh conditions and with high costs. Here, we used multi-source remote sensing and field surveys to quantify the changes in an RTS on Eboling Mountain in the Qilian Mountain Range in west-central China. Based on optical remote sensing and SBAS-InSAR measurements, we analyzed the RTS evolution and the underlying drivers, combined with meteorological observations. The RTS expanded from 56 m^2 in 2015 to 4294 m^2 in 2022, growing at a rate of 1300 m^2/a to its maximum in 2018 and then decreasing. Changes in temperature and precipitation play a dominant role in the evolution of the RTS, and the extreme weather in 2016 may also be a primary contributor to the accelerated growth, with an average deformation of −8.3 mm during the thawing period, which decreased slope stability. The RTS evolved more actively during the thawing and early freezing process, with earthquakes having potentially contributed further to RTS evolution. We anticipate that the rate of RTS evolution is likely to increase in the coming years.

Keywords: retrogressive thaw slump (RTS); InSAR; permafrost; Qilian Mountains [38.0030, 100.8867]

check for updates

Citation: Liu, X.; Peng, X.; Zhang, Y.; Frauenfeld, O.W.; Wei, G.; Chen, G.; Huang, Y.; Mu, C.; Du, J. Observed Retrogressive Thaw Slump Evolution in the Qilian Mountains. *Remote Sens.* **2024**, *16*, 2490. https://doi.org/10.3390/rs16132490

Academic Editor: Alexander Kokhanovsky

Received: 16 May 2024
Revised: 5 July 2024
Accepted: 5 July 2024
Published: 7 July 2024

1. Introduction

Due to climate change, the rate of high-elevation warming has been twice as fast as the global rate [1]. Over the past 50 years, the Tibetan Plateau has experienced significant warming and thinning of permafrost, a decrease in the area of permafrost [2], an increase in active layer depth [3], an increase in the frequency of surface freezing and thawing, and a decrease in the number of freezing days [4,5]. The degradation of permafrost over the years has exacerbated the occurrence of thaw-related hazards [6,7], which will have a significant impact on infrastructure, the ecological environment, and safety. Permafrost degradation induces the development of various thermal/thaw phenomena due to the combined influence of continued global warming and increasing engineering activities [8,9]. In relatively flat terrains, the main manifestations are thermokarst lakes and ponds, thawing ditches, and thaw settlement. On slopes, however, destabilization can result in active layer slides, retrogressive thaw slumps (RTSs), and mudflows [9]. The occurrence and formation of RTS could influence the thermal status of permafrost, local ecology, and infrastructure. Through ground temperature monitoring, field studies found that the shallow ground temperature in the area of active layer slippage was significantly higher than in nearby undisturbed areas [9]. The surface of RTS is exposed for a long time, and it is difficult to recover any vegetation, affecting the regional ecological environment. Furthermore, the formation and expansion of RTSs expose organic matter in the soil as well as subsurface ice, accelerates the release of CO_2 and CH_4, and significantly impacts regional and global climate change [10]. Therefore, monitoring and assessing RTSs are particularly important.

Most previous work has focused on the identification of RTSs and detecting changes. For identification, the primary methods include visual interpretation, deep learning based on imagery, and field verification. For example, Huang et al. [11,12] applied deep learning to extract feature information and attempted to identify RTSs based on remote sensing images in the Beilu River area. For quantifying changes, multi-period remote sensing images have been used to monitor RTSs, their rates of change, and even their volume. Based on long time series of remote sensing data, Antoni et al. [13] investigated changes in RTSs and the relationship between their rate of formation with a warming climate during summer on Banks Island in Northern Canada and found a relationship with increasing summer temperature. Swanson et al. [14] analyzed the effect of permafrost degradation on slope stability in Alaska's Arctic National Park by comparing the changes in RTS development, active layer slides, and frozen rock debris creep slides in the region over three time periods, and they found that permafrost thawing in mountainous regions may cause a variety of new slope failures.

While previous work has focused on the identification, changes, and environmental influences of RTSs, outstanding knowledge gaps are the changes in RTS's freeze–thaw processes and their potential influences, specifically in the Qilian Mountains on the northeastern edge of the Tibetan Plateau. Thus, we identify an RTS in the Qilian Mountain permafrost zone by using five high-resolution remote sensing images and, combined with field verification, monitor the evolution of the RTS at high temporal resolution and long time series using small baseline subset interferometric synthetic aperture radar (SBAS-InSAR). Meteorological station observations and seismic data for the area are used to analyze the deformation characteristics of the freeze–thaw process during the development of the RTS. The ultimate goal of this study is to determine the potential factors that drive RTS development and to provide baseline data and theoretical support for ecological research on these landform features.

2. Study Area

A specific RTS site within the permafrost region of Eboling Mountain in the upper Hei River basin of the Qilian Mountains was chosen as the focal point of this investigation (Figure 1). The permafrost region within the Hei River basin spans approximately 14,100 km^2, constituting approximately 10.3% of the basin's total area [15]. In the upper reaches of the Hei River, the average annual temperature remains below 2 °C, with precipitation predominantly occurring during the summer months. Ground temperature, measured at 16 m, generally exceeds -2 °C across much of the permafrost area [16]. Notable disparities exist between the southern and northern slopes, with the lower boundary of permafrost and mean annual ground temperatures markedly higher in the south.

According to field observations, the elevation limit of permafrost in Eboling Mountain is about 3400 m [17]. Permafrost is primarily located in peatlands with high water contents [17,18]. Analysis of borehole samples from the area reveals a predominant peat-clay soil composition, with rich organic matter content and high soil moisture, as well as the presence of abundant ground ice [18]. The prevailing vegetation type comprises alpine swampy meadows, covering extensive areas. The distinctive combination of topographical features, vegetation, and soil properties in this region, in addition to the ongoing degradation of permafrost and subsequent ice melt, has contributed to various landscape features.

These include characteristic micro-geomorphic formations such as grassy pingos, thaw depressions, and RTSs.

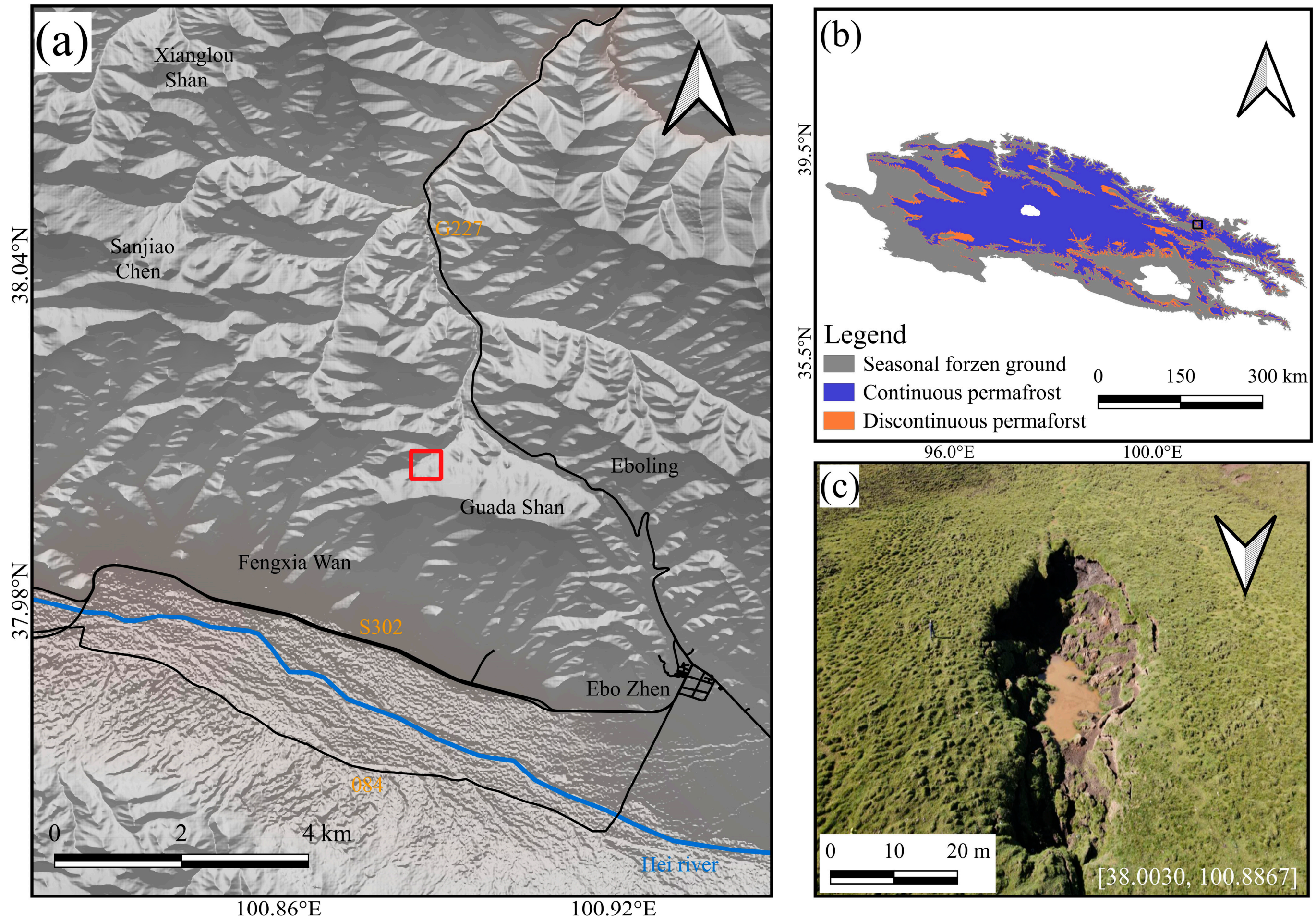

Figure 1. Study area indicating (**a**) the location of the RTS (red rectangle) on a hill-shaded DEM showing mountains, rivers, and roads in our study area. (**b**) The distribution of permafrost and seasonally frozen ground in the Qilian Mountains [19] where the black rectangle presents the location of our study area. (**c**) An unmanned aerial vehicle photograph of the RTS, with the white arrow denoting the direction of the RTS movement.

3. Data and Methods

3.1. Data

3.1.1. Synthetic Aperture Radar Data

To study the evolution of this RTS, we selected a total of 209 Sentinel-1A images from 5 July 2015 to 5 June 2023. This dataset covers a duration of 8 years and encompasses single-look complex data, facilitating the acquisition of both phase and amplitude information. The images were acquired in interferometric wide mode with a vertical–vertical polarization configuration. Sentinel-1 images have a temporal resolution of 24 days from 5 July 2015 to 31 January 2017 and 12 days thereafter. Imagery for 60 days is missed from 8 June to 7 August 2020.

3.1.2. Optical Remote Sensing Images

To comprehensively capture the evolution of this RTS, we employed five high-resolution optical remote sensing images to examine its morphological and area changes over time (Table 1). Specifically, Pleiades-1 imagery was obtained via Google Earth, and Geo-Eye-1 imagery was obtained via ESRI World Imagery Wayback.

Table 1. High-resolution optical remote sensing image datasets.

Sensor	Resolution (m)	Acquisition Date
Pleiades-1	0.50	14 August 2015, 16 July 2017, 23 August 2018, 28 February 2020
GeoEye-1	0.48	27 October 2022

3.1.3. In Situ Observations

A meteorological observatory is located within 100 m of the RTS and provides average daily air temperature to calculate the annual average temperature and freeze–thaw index, daily precipitation data to determine the effect of precipitation on the development of the RTS at different times, 5 cm soil temperature to differentiate between the freezing and thawing periods of the RTS in different years, and 20 cm soil moisture to quantify the effect of soil moisture on the activity of the RTS. Any missing temperature data were interpolated using data from a Chinese Meteorological Administration (CMA) weather station located 70 km from the RTS. These data have been quality controlled, and the station dates back to the 1950s and 1960s. To ensure the accuracy of the interpolated results, monthly average air temperatures (MAATs) and annual average air temperatures were also calculated based on daily air temperatures. The interpolated results are closely correlated with the observations, with regression coefficients greater than 0.95.

3.1.4. Earthquake Observations

To investigate the potential influence of earthquakes, seismic data with a magnitude greater than 4 in the vicinity of this RTS during the time frame of the study were obtained from the China Earthquake Networks Center.

3.2. Methods

3.2.1. Mapping of RTS from Optical Remote Sensing

Field surveys indicated that this RTS is characterized by a collapsed body, encompassed by tension cracks. To facilitate a more precise quantification of the RTS evolution, we delineated vector boundaries of the RTS on various images using manual visual interpretation in ArcGIS 10.8. This process involved accurate image alignment and enabling the generation of shapefile files, from which we calculated the area of the RTS.

3.2.2. Ground Deformation Derived from InSAR

We apply the SBAS-InSAR method to detect ground deformations in the RTS and monitor changes during the freeze–thaw process. The active layer, characterized by frost heave and thaw settlement [20], exhibits extensive surface deformation during the freeze–thaw cycle and is, thus, monitored using InSAR. SBAS-InSAR is specifically a time-series processing technique. Usai et al. [21] first established a series of interferograms characterized by small spatiotemporal baselines, employing a least-squares method to extract time-series cumulative deformation. However, the formation of multiple baseline subsets introduces rank deficit issues during the least-squares solution process. Berardino et al. [22] introduced the singular value decomposition (SVD) algorithm to address these rank deficit problems, thus establishing the classic SBAS method. This approach requires multiple SAR images from the same region at different times and selectively extracts radar signals with stable scattering, achieving higher accuracy [23]. Therefore, it is a reliable method for monitoring slow ground displacements. With the increasing number of satellite-based SAR instruments, a growing volume of SAR image data are available for InSAR processing to monitor changes on the Earth's surface [23,24].

We used ENVI SARscape (version 5.6.2), which automatically designates regions that meet specified criteria as Ground Control Points (GCPs). During the optimization and reflating phases of the initial and subsequent inversions, criteria, including coherence, amplitude divergence index, model displacement rate, and residual topography, are integrated to identify stable regions. Regions characterized by high coherence and minimal residual topography are delineated as stable areas, generating corresponding mask files. These mask files are subsequently applied to interferograms from each deconvolution process to select valid reference points (GCPs), based on the coverage of stable regions within each interferogram.

Upon importing SAR data into SARscape, a header file is generated to facilitate the calculation of multi-look views based on oblique distance resolution, azimuth resolution, and incidence angle information. The dataset used had an incidence angle of 34.17°, a distance sampling interval of 2.33 m, and an azimuth sampling interval of 13.97 m. Consequently, we derived a distance look count of 1 and an azimuthal look count of 3. Given the images' higher temporal resolution and good correlation, the maximum normal baseline is set to 2% and the maximum temporal baseline to 90 days.

In applying InSAR, the coherence coefficient is a crucial parameter that indicates the level of coherence. Using the coherence coefficient as a threshold to remove areas of low coherence can improve monitoring accuracy [24]. Generally, if the coherence is less than 0.2, measurement precision decreases [24,25]. For the completeness of our results, we set the coherence coefficient threshold to 0.1 during the interferometric process, to ensure the accuracy of the results. However, the actual results show that the coherence coefficients for RTS and its surroundings are all greater than 0.2. In the northern part of RTS, the coherence coefficient reaches 0.6, ensuring the reliability of our study results.

We utilized a 10 m resolution Copernicus DEM product to correct the topographic phase in each interferogram. The Delaunay minimum cost flow method was employed to unwrap all interferograms. The final results depict the line-of-sight deformation of the RTS from July 2015 to June 2023. Due to the limitations of field surveys and the focus of this study on investigating the development process of the RTS, we did not conduct ground measurements to validate the obtained results.

3.2.3. Freezing/Thawing Index

As in Frauenfeld et al. [26], we sum all temperatures below or above 0 °C during the freezing or thawing periods to calculate the freezing/thawing index [27,28]. We define the freezing period to be from July to June of the following year to sum the freezing index during a continuous cold season. The thawing period is defined as from January to December [27,29]. When MMAT was below 0 °C, we multiplied the absolute value of the MMAT by the number of days within that month and then summed the monthly freezing index values over the calendar year. The same approach is applied for the thawing index during the thawing period. The annual freezing/thawing index based on monthly data is, thus, as follows:

$$\mathrm{FI} = \sum\nolimits_{i}^{N_T} |T_i| \times D_i, \ \ T_i < 0\,^\circ\mathrm{C}, \tag{1}$$

$$\mathrm{TI} = \sum\nolimits_{i}^{N_T} T_i \times D_i, \ \ T_i > 0\,^\circ\mathrm{C}, \tag{2}$$

where T_i is mean air temperature for the month, D_i is the number of days in that month, the freezing period is $i = 1, 2 \ldots N_T$, and the thawing period is $i = 1, 2 \ldots N_T$.

3.2.4. Additional Processing

In the time-series deformation results obtained from SBAS-InSAR, the deformation of all images is relative to the first image and, therefore, requires the deformation and deformation rate for a certain period. Assuming that the deformations in the two images are A_1, A_2 relative to the first image (A_2 is imaged later than A_1), and the imaging times of the two images are t_1 and t_2, the deformation and the deformation rates from t_1 to t_2 are:

$$A_2 - A_1, \tag{3}$$

$$A_2 - A_1 / t_2 - t_1, \tag{4}$$

4. Results

4.1. RTS Development

The boundaries of the RTS in the remote sensing images corresponding to different periods were delineated, and the RTS area was calculated (Figure 2). The area was only 55.5 m^2 in 2015, indicating that it was in the early stage of formation. From 2015 to 2017, the RTS began to develop from the south, and slumps began to appear in the center. However, the development was slow, with a growth rate of 146 m^2/a.From 2017 to 2018, slumps in the south continued to develop and converged. The collapse in the central region rapidly extended northward, resulting in a rapid overall increase in slump area and a growth rate of 1263.8 m^2/a, 8.6-times greater than before, entering the middle stage of development. Between 2018 and 2020, the slumps in the central and southern regions converged and extended overall to the north and south, with a growth rate of 870.5 m^2/a, somewhat reduced but still at a high rate of growth. From 2020 to 2022, there was little change in the north–south extent, but the RTS began to widen in the east–west direction at a growth rate of 465.4 m^2/a, beginning to decrease and gradually entering a late stage of development. Overall, the area of the RTS increased from 55.5 m^2 to 4293.7 m^2 at an average growth rate of 587.7 m^2/a, with an initial trend of slow growth, then accelerated growth, followed by gradual slowing. The overall shape evolved from initially small blocks to a tongue shape extending north and south for 319 m, with development initially beginning in the south, followed by concurrent development in the south and central regions, with the central to northern extent being greater than that to the southern regions, followed by convergence and continued development and eventually widening in the east–west direction.

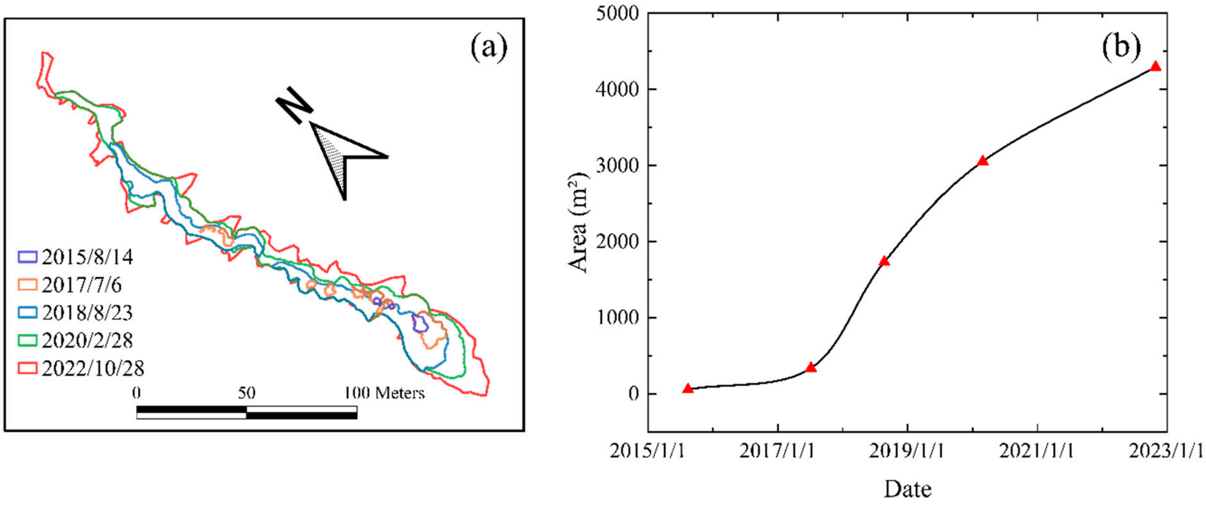

Figure 2. (**a**) RTS boundaries from five different periods, represented by lines of different colors and (**b**) RTS area change curve. The red triangles represent the time at which we obtained the images.

4.2. Ground Deformation Changes

Permafrost is composed of two layers: an active layer underlain by a frozen layer. The frozen layer remains above or below 0 °C for two or more consecutive years, while the active layer is the soil layer close to the surface, which thaws in summer and freezes in winter [30]. When the soil temperature drops below freezing, water in the soil pores freezes and expands, causing the unfrozen water to migrate towards the freezing edge and eventually freeze, resulting in frost heave. During the thawing process, pore water is discharged, causing the soil to sink. This phenomenon is known as thaw settlement [20].

To better characterize the evolution of the RTS, we selected an area outside the RTS for comparison with the deformations observed inside the RTS. We found that the RTS exhibits a significantly greater settlement than the external area by 20–30 mm (Figure 3). The deformation shapes inside and outside the RTS are relatively similar; however, upon closer inspection, both thaw settlement and frost heave effects are less pronounced inside

RTS compared to the external environment, with smaller deformation amplitudes. This may be attributed to changes in the mechanical properties of the surface soil on the RTS relative to the surrounding permafrost. Additionally, both inside and outside the RTS, there were numerous instances of abrupt settlements (or heaves), likely corresponding to periods of RTS development and expansion.

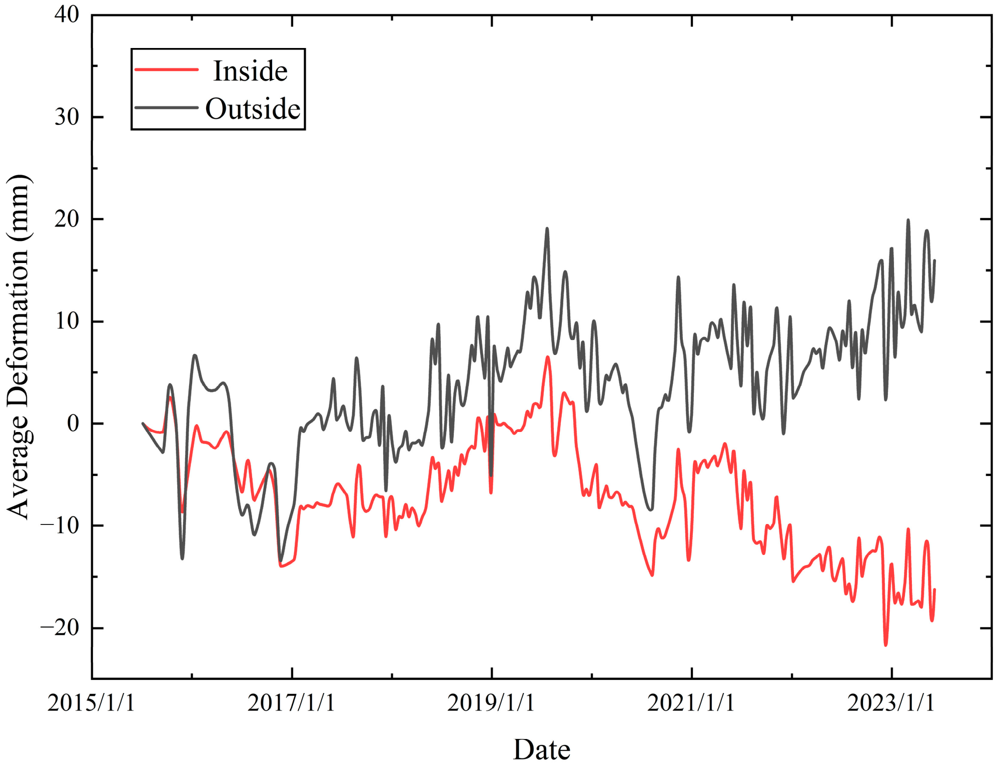

Figure 3. Deformation time series inside and outside RTS from 5 July 2015 to 5 June 2023.

Our study utilizes weather station data to distinguish between freezing and thawing periods each year, using a 5 cm soil temperature of 0 °C as the boundary. Combining the cumulative deformations during the thawing period (Figure 4), it is evident that the deformation is mainly negative (indicating settlement) or close to 0. In 2016, significant subsidence was observed in the northern part of the RTS, and in 2021, in the southern part of the RTS, with subsidence magnitudes reaching 18 mm and 21 mm, respectively, higher than the surrounding areas. Additionally, during the 2018 thawing period, significant uplift reaching 13 mm was noted in the central and southern parts of the RTS, possibly due to accumulation caused by collapse of the peripheral soil. In 2017 and 2019, overall subsidence occurred in the southern part and uplift in the northern part of the RTS, indicating extensive surface permafrost thawing and the accumulation of meltwater, leading to parallel sliding along the slope surface. A similar situation occurred in 2020, when westward sliding resulted in predominant subsidence of 15 mm in the western part of the RTS, and uplift of 16 mm in the eastern part.

The summary statistics of RTS deformation (Figure 5) indicate that in 2015, during the early stage of RTS evolution, thaw settlement was moderate but with a large number of negative outliers, indicting sinking. Substantial sinking occurred in 2016, with a mean and median value of deformation of −8.3 mm. Combined with the spatial map (Figure 4b), thaw settlement is evident across much of the RTS area. The central and northern parts of the RTS were not yet developed at that time. The creep rate of the landslide-affected slopes is significantly higher than that of natural slopes [31]; therefore, the stability of the central and northern portion of the RTS decreased during the thawing process in 2016. The mean and median values of deformation in 2017–2020 were relatively stable, and the number of deformation outliers was higher in 2018. Combined with the results of the analysis of the area change, 2018 was the fastest year during the evolution, and the stability decreased. A large number of deformation outliers were, again, seen in 2021. In combination with the spatial map (Figure 4g), it can be concluded that the greatest thaw settlement was in the south-central part of the RTS, and the area changes (Figure 2) show that the south-central part of the RTS is widened at this stage.

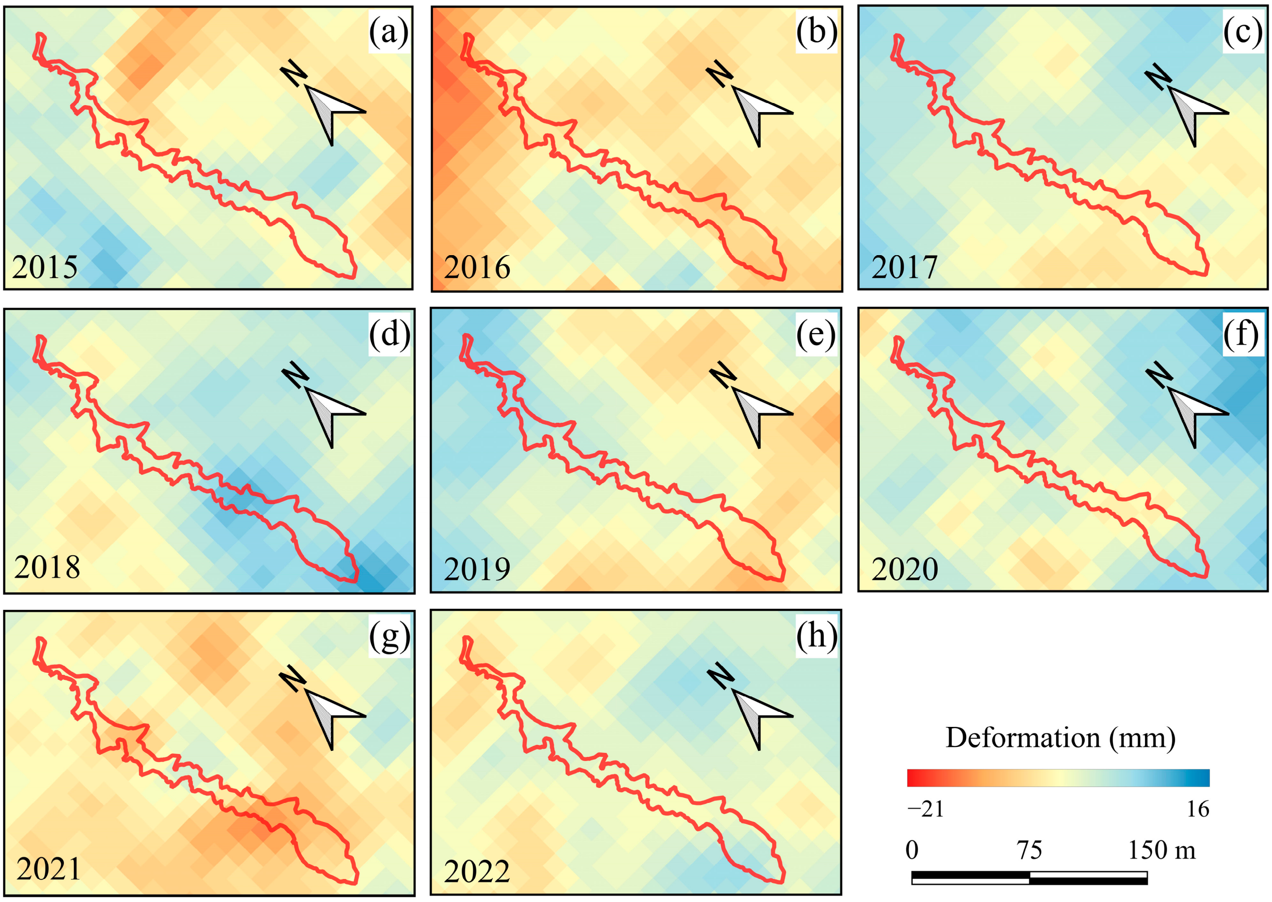

Figure 4. The amount of deformation during the thawing period from (**a**–**h**, 2015 to 2022) . Due to image date constraints, the thawing period in 2015 started on July 5.

To examine the overall evolution of the RTS during different stages of the thawing period, we averaged all pixels within the RTS (Figure 6). At the onset of thawing, the soil temperature fluctuated around 0 °C, resulting in alternating freezing and thawing, leading to both upward and downward deformations ranging from 0.2 mm to 3.7 mm. As the thawing period progressed and temperatures rose, soil temperature remained consistently above 0 °C, causing a rapid decline in deformation, with thaw settlement being most pronounced and reaching a maximum of 237.3 mm. Subsequently, as the active layer deepened, RTS development commenced, triggering collapses of surrounding thawed soil, which accumulated within the RTS. This led to an upward deformation, followed by subsequent sinking as the collapsed soil thawed. Towards the end of the thawing period, soil temperatures decreased and fluctuated above and below 0 °C, with freeze–thaw processes alternating. Considering the different stages of the RTS, the deformation changes from 2015 to 2017 were relatively consistent, indicating normal developmental stages, with an overall deformation of -5.3 mm during the thaw period in 2016 (Figure 6a–c). However, in 2018, RTS deformation fluctuations exhibited marked oscillations, experiencing multiple changes and thawing, with rates of up to 70 mm/a (Figure 6d). This suggests an accelerated expansion of the RTS area at this time, consistent with previous findings. Similarly, deformation fluctuations in 2021 and 2022 were large, with cumulative deformation during the 2021 thawing period being −5.1 mm (Figure 6g,h), similar to 2016 and potentially leading to further slope instability. Hence, we hypothesize that the RTS in future years is more likely to experience increased growth rates.

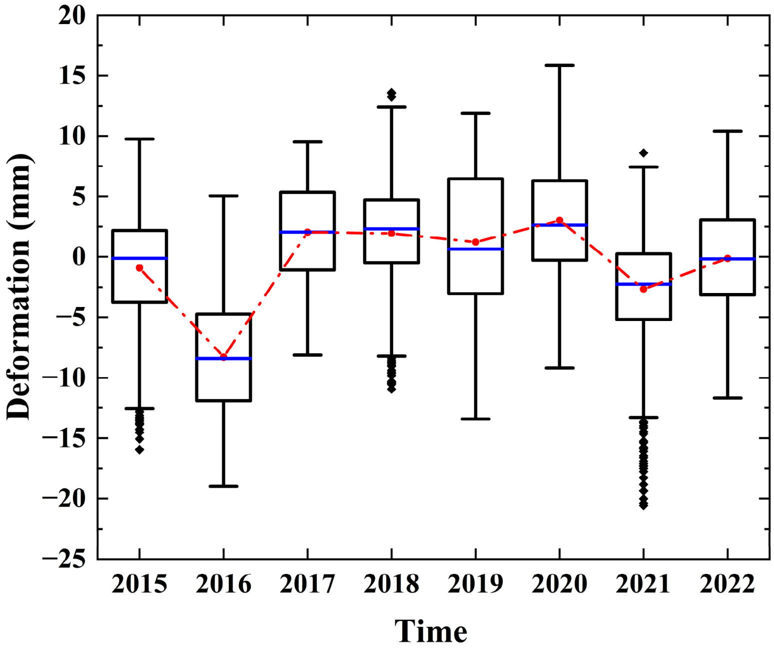

Figure 5. Deformation magnitude of all pixels in and around the RTS (see domain in Figure 4) during the thawing process. The boxes contain 50% of the pixels and the lower line and the upper line correspond to 25% of the pixels, respectively. The blue line is the median value and the red point is mean value. Black points indicate outliers, deviating from three standard deviations.

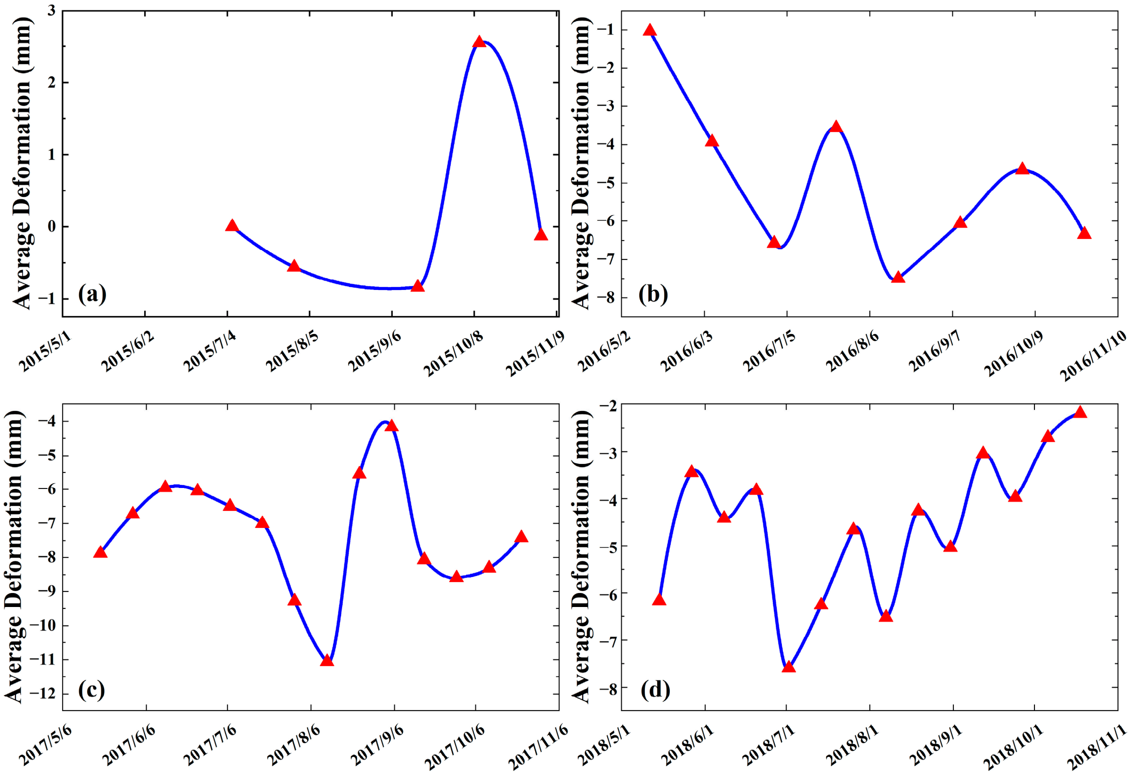

Figure 6. *Cont.*

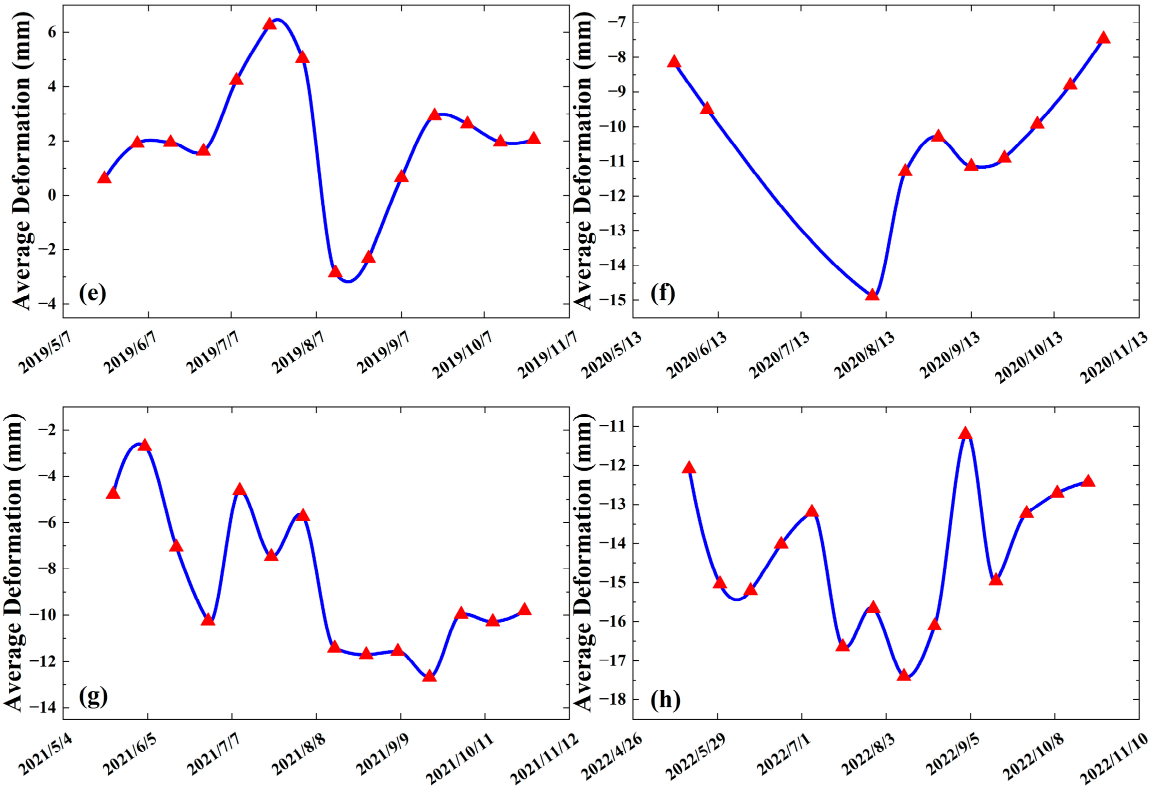

Figure 6. (**a**–**h**) Time series of the average deformation of the RTS and its surrounding area during the thaw process. The periods corresponding to **a**–**h** are the same as in Figure 4.

During the freezing period (Figure 7), deformations were mostly near and above 0. The degree of deformation within the RTS is significantly lower compared to the surrounding areas, maintaining a relatively stable state, as previously observed (Figure 3). However, despite this, there was subsidence of 15 mm in the central part of the RTS in 2016 (Figure 7b), and significant subsidence occurred in the region in 2019, with a deformation of −21 mm (Figure 7e). In the early stages of RTS development, from 2015 to 2017, many negative outliers are evident (Figure 8). There was a substantial overall subsidence, with the mean value decreasing from 3.6 mm in 2018 to −10 mm in 2019. Subsequently both the median and the mean value increased each year, with a small number of subsidence anomalies occurring in 2020 and 2021. During the freeze period, substantial settlement occurred during early freezing when the active layer was not completely refrozen, followed by subsidence during the later freeze period, or by sliding due to a warm winter when the surface soil across the area was not frozen, and subsurface ice provided a good sliding surface.

By analyzing the temporal change in average deformation during the freeze period (Figure 9), in all years, subsidence occurred in October to January of the next year, when in the early freeze period, and the amount of settlement was in the range of 7–12 mm. This may be due to the fact that at this time, the temperature of the surface soil fluctuates above and below 0 °C, and ice and water coexist in the soil, providing a good lubricating surface in the surface soil. The soil is not completely frozen and has poor shear resistance, leading to various amounts of active layer sliding.

In general, after January, soil strength increases and RTS deformation decreases and remains largely unchanged, and deformation enters a stable period. Frost heave is most pronounced before the start of this period, with a maximum increase of 10.2 mm (Figure 9f). At the end of the freeze period, soil temperatures rise to near 0 °C, and the soil freezes and thaws alternately, with small fluctuations in deformation.

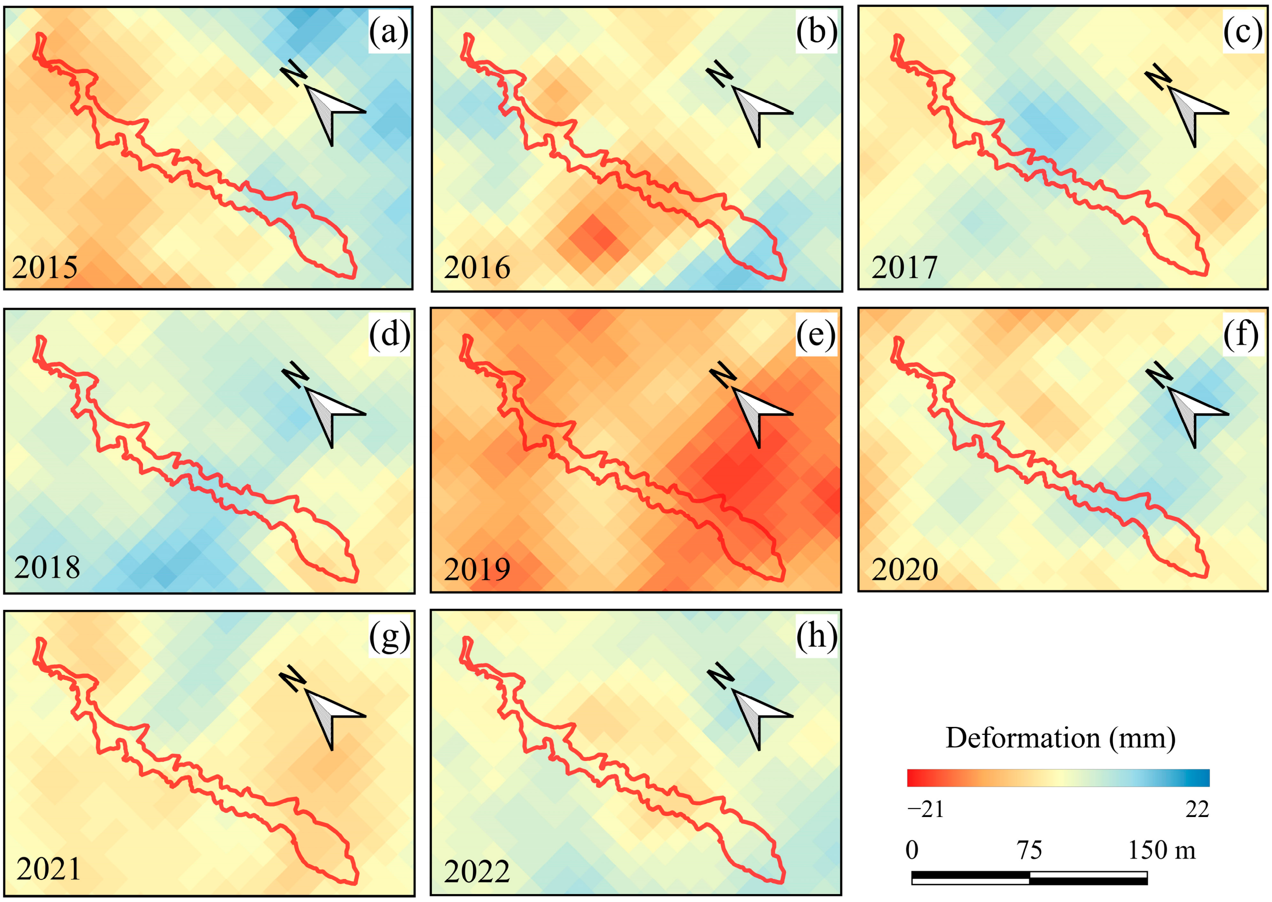

Figure 7. The amount of deformation during the freeze process from (**a**–**h**, 2015 to 2022). The red contour line is the shape of the RTS on 28 October 2022, and the contour lines of different colors correspond to the shape of RTS in different periods.

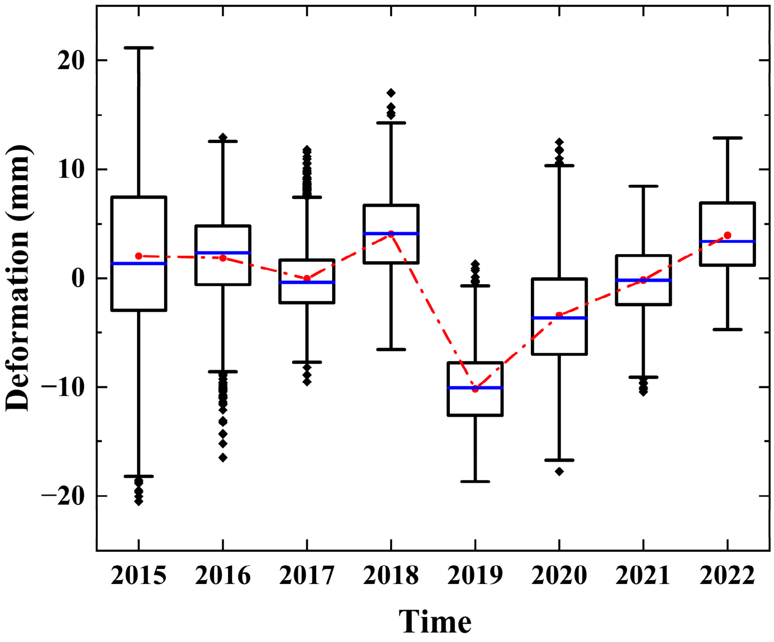

Figure 8. As in Figure 5, but during the freeze period.

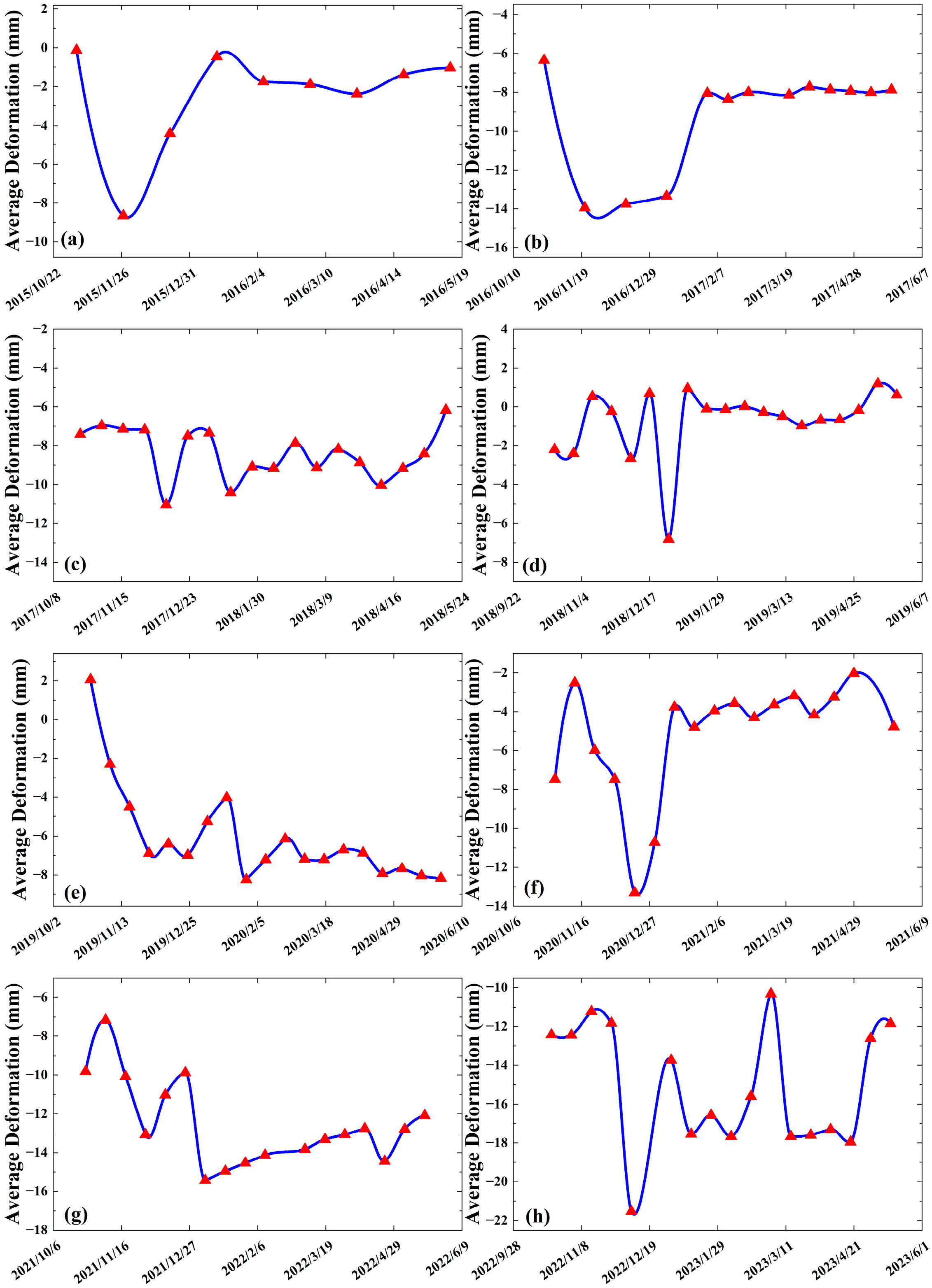

Figure 9. (**a**–**h**) Time series of the average deformation of the RTS and its surrounding area during the freezing period. The periods corresponding to **a**–**h** are the same as Figure 8.

The overall 2015–2023 evolution of the RTS during the freezing period was characterized by consistent deformation changes during the early stages, and the freezing stages were easily distinguishable (Figure 9a,b). In the following years of accelerated RTS development, the deformation fluctuations during the freeze period increased, while the fluctuations during the stabilizing period became shorter. The effect of frost heave was weaker during the freeze periods in 2017, 2019, and 2021. This might have been caused by the increase in soil-free faces and collapse under the combined effect of warm winters and increased RTS area. The fluctuation in RTS activity during the freeze period of 2021 and 2022 was still significant, indicating a possibility of accelerated development of the RTS.

5. Discussion

5.1. The Potential Driving Factors

5.1.1. Climate Factors

In general, precipitation increases soil saturation and pore pressure, which increases the likelihood of slope failure [32], and widespread or extreme precipitation increases the area of the RTS [33–35]. To assess the impact of precipitation events on the evolution of this particular RTS, we utilized data from meteorological stations. Omitting years with missing data, we selected the four years of 2016, 2017, 2018, and 2019 when the RTS was more developed. Based on data from the meteorological observatory, the rainy season with more frequent precipitation occurs from the beginning of April to the end of October. The variability in precipitation from 2016 to 2019 was large, with annual precipitation reaching 544.4 mm in 2016 and only 390.5 mm in 2018. Additionally, extreme precipitation with a daily total of 44.6 mm was observed on 21 August 2016, which was the highest daily precipitation recorded during the period.

The precipitation in 2016 was characterized by both high short-term and total precipitation (Figure 10a). The sudden extreme precipitation caused a drastic change in the precipitation pattern during the thaw period, which greatly interfered with the development of the RTS. Combined with the boxplot (Figure 5), we find that the mean value of subsidence in 2016 was the lowest value from 2015 to 2022, reaching 8.3 mm. The subsequent three years, on the other hand, were relatively stable in terms of precipitation and deformation mean, with deformation outliers only occurring in 2018, suggesting that the RTS most likely had its fastest rate of development in 2018.

Given that the RTS did not develop at an accelerated rate in 2016, the extreme precipitation event in that year was not the direct cause of prompting the development of the RTS. However, this event had a non-negligible effect on the development of the RTS, and we hypothesize that this event led to a rapid increase in subsurface saturation and increased pore water pressure, thus decreasing the shear strength of the soil. This, in turn, increased the thickness of the active layer and, ultimately, decreased the stability of the slope. This induced the RTS to accelerate its development in 2017 and 2018.

Climate warming and disturbance may impact permafrost stability in cold environments [36,37]. Rocks are held together by ice filling their cracks and crevices. Freeze–thaw processes are characterized by fluctuations in subsurface temperature and moisture content, which can result in substantial changes in shear strength (cohesion and friction angle) and can drive landslide initiation [38]. The transition from perennially frozen to seasonally frozen ground accelerates the effect of freeze–thaw processes on both bedrock and unconsolidated material [39]. As the air temperature increases, the permafrost warming and thawing may weaken rock faces and the inherent stability, leading to the slope failure [40]. In mountain permafrost regions, such as the European Alps, Canada, and the Tibetan plateau, researchers have observed a growing trend of landslide activity due to climate change [12,41,42].

The mean annual air temperature in the region was relatively stable from 2015 to 2022 (Figure 11a). However, it is worth noting that the temperature in 2016 and 2022 was −2.4 °C and −2.27 °C, respectively, which is 0.17 °C and 0.3 °C above the average (dashed line, Figure 11a). This was followed by a decrease from 2016 to 2019, with a 2019 temperature of −2.82 °C, which is 0.25 °C below the average. Notably, large temperature fluctuations can exacerbate the freeze–thaw cycle, thus impacting the stability of the RTS.

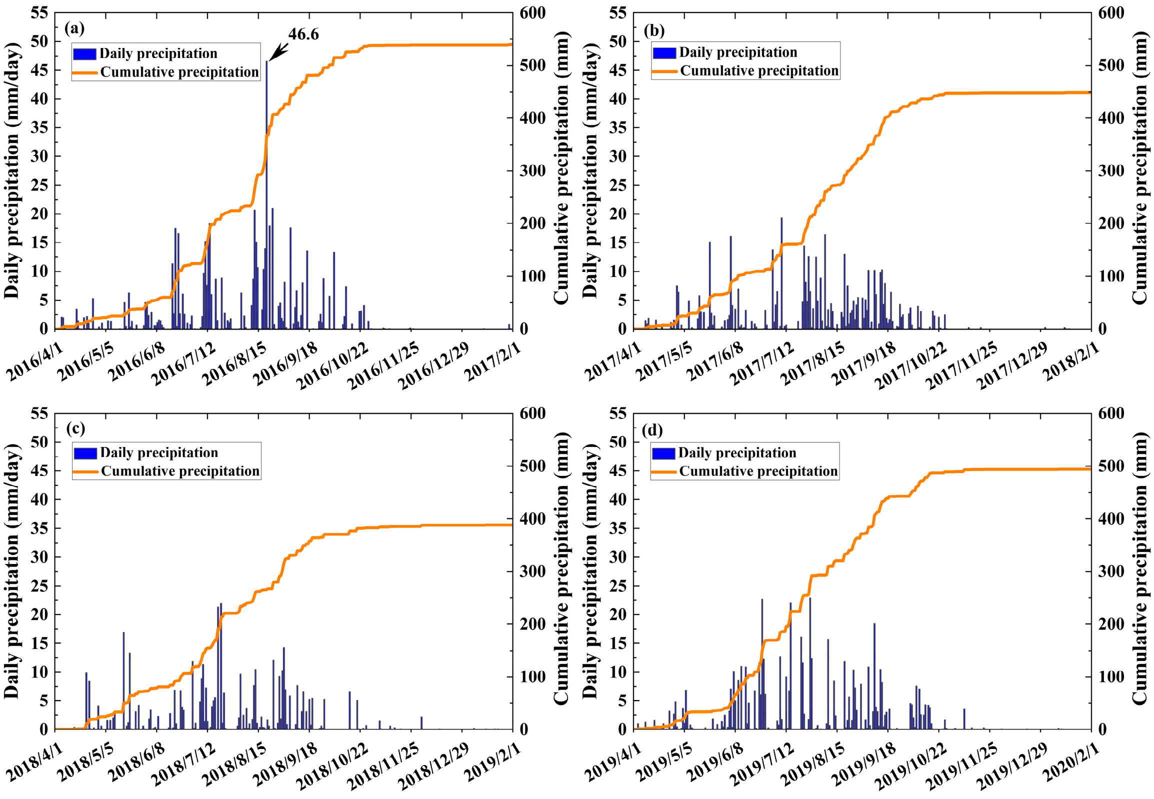

Figure 10. Daily precipitation amounts and cumulative precipitation curve from (**a**–**d**, 2016 to 2019). We defined the rainy season as starting on 1 April, based on meteorological data from the observing station.

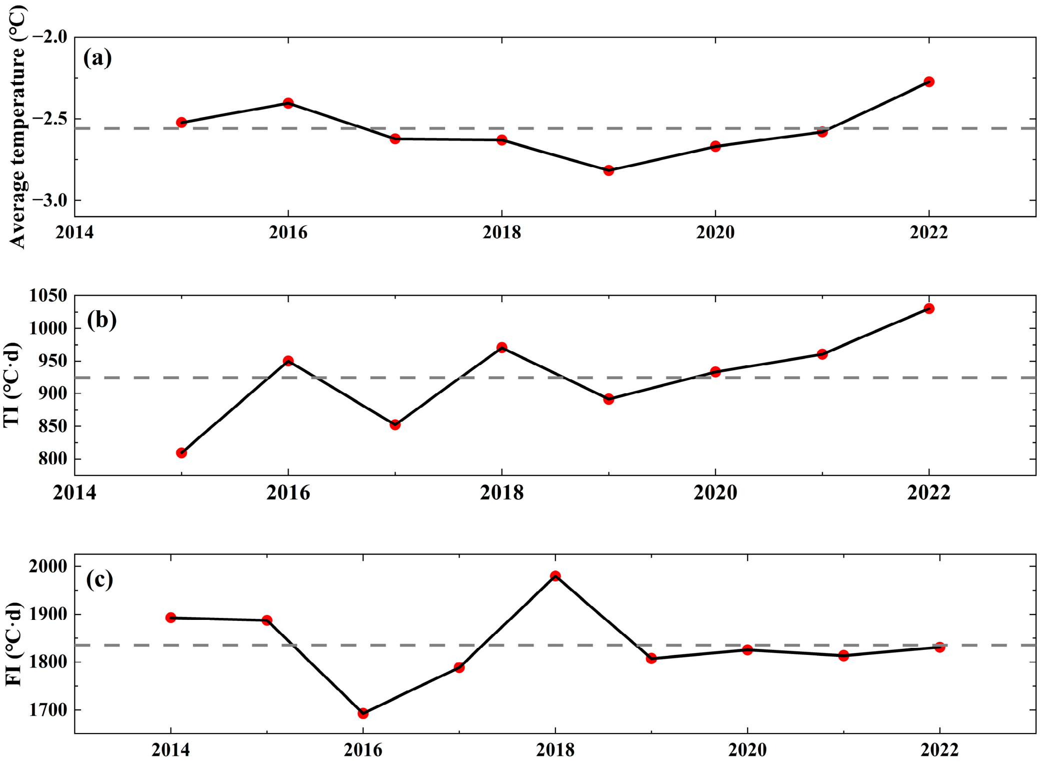

Figure 11. (**a**) Mean annual air temperature, (**b**) thawing index, and (**c**) freezing index from 2015 to 2022.

The TI shows a clear upward trend from 2015 to 2022 (Figure 11b), with high variability from 2015 to 2019, followed by a steady yearly increase, reaching 1030 °C·d in 2022. Conversely, the FI dropped to 1693 °C·d in 2016 (Figure 11c), indicating a warmer winter that may slow the freeze–thaw cycle and keep the soil moisture unfrozen for an extended period, thereby reducing RTS stability [35]. The FI increased to 1980 °C·d in 2018 and remained stable from 2019 onwards, suggesting temperature instability from 2015 to 2019, which might have exacerbated RTS development.

In 2016, the air temperature, TI, and FI were all higher than the average and variable. Combined with extreme precipitation events, the extreme climate in 2016 likely triggered the accelerated development of the RTS.

5.1.2. Freeze–thaw Process

This RTS began developing in 2015. According to existing research [9,43], we posit that exposed slopes led to thawed soil collapse at the exposed faces. After the collapse, thick layers of ground ice became partly or fully exposed or their soil cover thinned, resulting in melting of the ground ice. RTS activity increased during the thawing and early freezing stages. Meltwater saturated the collapsed soil mass, putting it in a saturated or supersaturated state. The surface of the ground ice provided a good sliding surface. Saturated and supersaturated soil, lubricated by water accumulated between the ice surface and soil layers, formed this RTS. Subsequently, this led to further cracking, collapsing, and sliding of the soil slope. The weather conditions in 2016 were characterized by drastic temperature fluctuations, exacerbating the RTS expansion, with rates reaching 1264 m^2 per year. Analysis of time-series data from 2021 and 2022, coupled with area growth rates, indicates that RTS development may further accelerate. Once reaching a certain scale, the soil accumulation at the forefront of the landslide will gradually stabilize as drainage, consolidation, and deepening of the ground ice melting surface progress.

We find that thawing proceeds more rapidly than freezing. As temperatures reach a certain point, the active layer begins to thaw, resulting in the discharge of pore water and frequent RTS activities. Conversely, freezing requires a preliminary phase before soil strength reaches a certain level and stabilizes. Qi et al. [20] observed that soil freezing undergoes a subcooling stage before reaching negative temperatures, transitioning the subcooled water into a sub-stable state, consistent with our study.

Soil moisture is a crucial factor that affects soil strength. Changes in water content and the freeze–thaw process alter the micro-structure of the soil, leading to changes in its mechanical properties [44]. Increased soil water content diminishes soil strength and bearing capacity, contributing to various deformation-related issues [20] and influencing RTS instability. For RTS, the primary source of soil moisture is meltwater. During the thawing period, soil moisture at a depth of 20 cm can peak at approximately 80%, while during freezing, it remains around 7%. Higher soil moisture correlates with increased temporal deformation risk. Conversely, decreasing soil moisture during freezing periods results in lower temporal deformation.

The impact of meltwater on the stability of collapse bodies involves two aspects: the influence on soil mass and stress conditions. Meltwater saturates the soil above the ice surface, resulting in saturated and supersaturated states. This change in soil moisture content generates pore water pressure buoyancy, ultimately weakening soil strength. Additionally, due to the weight of the soil water, the buoyancy force during infiltration reduces effective stress, causing stress adjustments that are detrimental to slope stability [45]. Therefore, changes in soil moisture directly contribute to RTS instability, while air temperature and precipitation indirectly affect RTS stability by modulating soil moisture levels.

5.1.3. Earthquakes

Earthquakes can affect permafrost temperatures by cracking and deforming permafrost ice, releasing moisture and heat [46]. The shaking can also cause liquefaction of sediments and expansion of soil materials, which allows for rapid infiltration of moisture, further affecting permafrost temperatures [47]. Earthquakes can change the friction at the base of the soil mass [48], leading to soil mass collapse and sliding within the RTS, which can promote RTS development.

To examine the impact of earthquakes on the development of this RTS, we gathered data for earthquakes with magnitudes greater than 4 in the vicinity of this RTS during the study period (Table 2). We analyzed the deformation of the ground surface before and after the earthquakes. Around the time of the earthquake occurrence, we collected SAR image data with a temporal resolution of 12 days. This high temporal resolution aimed to ensure that seismic deformation was the primary influencing factor during this period. Additionally, due to the uncertain impact of earthquakes on deformation, our study utilized the range of deformation to explore this potential influence (Figure 12). It was discovered that earthquakes have a higher probability of impacting the RTS during the thawing and early freezing periods. An earthquake on 9 August 2019 resulted in a significant deformation rate of −517 mm/a in the southern part of the RTS. This may be due to the active layer being unfrozen during this period, resulting in weakened soil strength and increased susceptibility to the effects of the earthquake. The instability of the area surrounding the RTS also impacts its development to some extent. The deformation rate in the western part of the RTS was −397 mm/a before and after the earthquake on 23 November 2015. Similarly, the deformation rate in the north-eastern part of the RTS was 372.6 mm/a before and after the earthquakes on 10 and 27 December 2022. During the middle and late freezing periods, the earthquakes' effects on the RTS were mitigated by increased freezing, soil strength, and decreased precipitation. Our results require further confirmation due to limited seismic data and the influence of factors, such as magnitude, depth, distance from the study area, and the period of occurrence.

Table 2. Seismic datasets in the study area.

Date	Epicenter [Latitude, Longitude]	Magnitude (M)	Depth (km)	Distance (km)
5 January 2023	[37.91, 101.13]	4.2	10	23.70
27 December 2022	[37.74, 101.3]	4.1	10	46.57
10 December 2022	[37.76, 101.26]	4.2	10	42.44
15 August 2022	[38.43, 99.26]	4.7	8	149.72
7 March 2022	[37.73, 101.44]	4.2	9	57.25
8 January 2022	[37.77, 101.26]	6.9	10	41.74
16 September 2019	[38.60, 100.35]	5.0	11	81.19
9 August 2019	[37.69, 101.59]	4.9	9	70.85
12 May 2019	[39.96, 100.58]	4.0	14	219.09
21 January 2016	[37.68, 101.62]	6.4	10	73.69
23 November 2015	[38.00, 100.40]	5.2	10	42.59

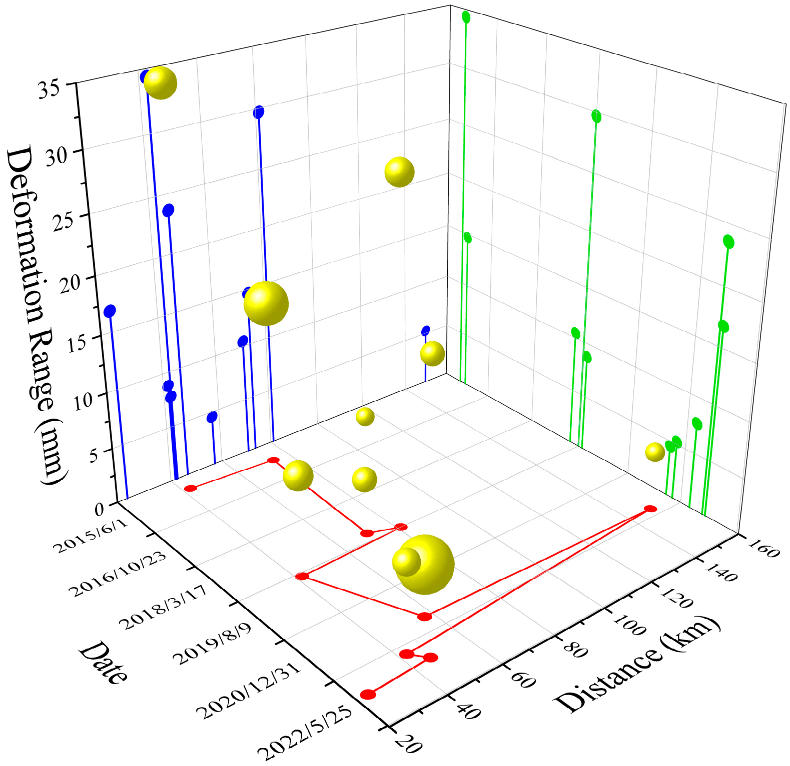

Figure 12. Here, we show a 2.5D map showing the earthquakes' impact on the RTS. The x-axis indicates the date of the earthquakes, the y-axis indicates the distance of the earthquake from the RTS, the z-axis indicates the shape-variable extreme deviation of the RTS and its surrounding area before and after the earthquake, and the size of the yellow sphere indicates the magnitude of the earthquake, with the larger the sphere, the greater the magnitude of the earthquake.

6. Conclusions

In this study, multi-source remote sensing images were used to study the spatial and temporal evolution of an RTS located on Eboling Mountain in the Qilian Mountains from 2015 to 2023. The RTS developed from an initial 55.5 m^2 in 2015 to 4293.7 m^2 in 2022, with the rate increasing and then decreasing, reaching a maximum in 2018, with a rate exceeding 1263.8 m^2/a. Meanwhile, remote sensing indicated the detail orientation of RTS development. During the thaw period, subsidence was relatively significant in 2016 and 2021, where the average subsidence in 2016 reached 8.3 mm, closely related to the extreme climate in 2016. During the freezing period, the surface soil was not completely frozen from the end of October to January, and the activities were more frequent; the frost heave was also the most significant. For the potential factors, the extreme weather in 2016 reduced the stability of the RTS slopes, leading to the rapid development of RTS slides in the aftermath. Earthquakes also have a potential effect on the RTS. Based on the analyses of the deformation curves and impacting factors, RTSs have the potential to develop at a faster rate in the coming years.

Author Contributions: Conceptualization, X.P., Y.Z., O.W.F. and J.D.; data curation, X.L.; formal analysis, X.L.; methodology, X.P., Y.Z. and J.D.; supervision, O.W.F.; visualization, X.L.; writing—original draft, X.L.; writing—review and editing, X.P., Y.Z., O.W.F., G.W., G.C., Y.H., C.M. and J.D. All authors have read and agreed to the published version of the manuscript.

Funding: This study was supported by the National Natural Science Foundation of China (grant No. 42161160328, 42171120) and the Fundamental Research Funds for the Central Universities (lzujbky-2021-72, lzujbky-2021-ct13).

Data Availability Statement: The Sentinel-1 dataset (https://asf.alaska.edu/ accessed on 8 August 2023), the Geo-Eye-1 imagery (https://livingatlas.arcgis.com/ accessed on 16 August 2023), and the earthquake data (https://news.ceic.ac.cn/ accessed on 5 October) are publicly archived datasets. The processed data used to construct the figures presented in this paper are available upon reasonable request from the corresponding author (pengxq@lzu.edu.cn).

Conflicts of Interest: The authors declare no conflicts of interest.

References

1. Wang, K.; Zhang, T.; Mu, C.; Zhong, X.; Peng, X.; Cao, B.; Lu, L.; Zheng, L.; Wu, X.; Liu, J. From the Third Pole to the Arctic: Changes and impacts of the climate and cryosphere. *J. Glaciol. Geocryol.* **2020**, *42*, 104–123.
2. Guo, D.; Wang, H. CMIP5 permafrost degradation projection: A comparison among different regions. *J. Geophys. Res. Atmos.* **2016**, *121*, 4499–4517. [CrossRef]
3. Guo, D.; Wang, H. Simulated historical (1901–2010) changes in the permafrost extent and active layer thickness in the Northern Hemisphere. *J. Geophys. Res. Atmos.* **2017**, *122*, 12285–212295. [CrossRef]
4. Peng, X.; Frauenfeld, O.W.; Cao, B.; Wang, K.; Wang, H.; Su, H.; Huang, Z.; Yue, D.; Zhang, T. Response of changes in seasonal soil freeze/thaw state to climate change from 1950 to 2010 across china. *J. Geophys. Res. Earth Surf.* **2016**, *121*, 1984–2000. [CrossRef]
5. Zhang, T.; Wang, K.; Zhong, X. Changes in the timing and duration of the near-surface soil freeze/thaw status from 1956 to 2006 across China. *Cryosphere Discuss.* **2014**, *8*, 3785–3809.
6. Harris, C.; Arenson, L.U.; Christiansen, H.H.; Etzelmüller, B.; Frauenfelder, R.; Gruber, S.; Haeberli, W.; Hauck, C.; Hoelzle, M.; Humlum, O. Permafrost and climate in Europe: Monitoring and modelling thermal, geomorphological and geotechnical responses. *Earth-Sci. Rev.* **2009**, *92*, 117–171. [CrossRef]
7. Genxu, W.; Yan, Y.; Guangtao, Z.; Ruiying, C. Cryosphere Ecosystems: Outpost and Barrier in Global Change. *Bull. Chin. Acad. Sci. (Chin. Version)* **2020**, *35*, 425–433.
8. Jin, H.; Li, S.; Cheng, G.; Shaoling, W.; Li, X. Permafrost and climatic change in China. *Glob. Planet. Chang.* **2000**, *26*, 387–404. [CrossRef]
9. Jing, L.; Fujun, N.; Zhanju, L.; Minghao, L.; Guo'an, Y. Development of thawing hazards and thermal influence on permafrost along Qinghai-Tibet engineering corridor. *J. Eng. Geol.* **2014**, *22*, 326–333.
10. Woods, G.C.; Simpson, M.J.; Pautler, B.G.; Lamoureux, S.F.; Lafrenière, M.J.; Simpson, A.J. Evidence for the enhanced lability of dissolved organic matter following permafrost slope disturbance in the Canadian High Arctic. *Geochim. Cosmochim. Acta* **2011**, *75*, 7226–7241. [CrossRef]
11. Zhang, E.; Liu, L.; Huang, L.; Ng, K.S. An automated, generalized, deep-learning-based method for delineating the calving fronts of Greenland glaciers from multi-sensor remote sensing imagery. *Remote Sens. Environ.* **2021**, *254*, 112265. [CrossRef]
12. Huang, L.; Luo, J.; Lin, Z.; Niu, F.; Liu, L. Using deep learning to map retrogressive thaw slumps in the Beiluhe region (Tibetan Plateau) from CubeSat images. *Remote Sens. Environ.* **2020**, *237*, 111534. [CrossRef]
13. Lewkowicz, A.G.; Way, R.G. Extremes of summer climate trigger thousands of thermokarst landslides in a High Arctic environment. *Nat. Commun.* **2019**, *10*, 1329. [CrossRef] [PubMed]
14. Swanson, D.K. Permafrost thaw-related slope failures in Alaska's Arctic National Parks, c. 1980–2019. *Permafr. Periglac. Process.* **2021**, *32*, 392–406. [CrossRef]
15. Wang, Q.; Zhang, T.-j.; Wu, J.; Peng, X.; Zhong, X.; Mu, C.; Wang, K.; Wu, Q.; Cheng, G. Investigation on permafrost distribution over the upper reaches of the Heihe River in the Qilian Mountains. *J. Glaciol. Geocryol* **2013**, *35*, 19–29.
16. Cao, B.; Zhang, T.; Peng, X.; Mu, C.; Wang, Q.; Zheng, L.; Wang, K.; Zhong, X. Thermal characteristics and recent changes of permafrost in the upper reaches of the Heihe River Basin, Western China. *J. Geophys. Res. Atmos.* **2018**, *123*, 7935–7949. [CrossRef]
17. Wu, J.-C.; Yu, S.; Yu, H.; Li, J.-P. Permafrost in the Middle-East Section of Qilian Mountains(II):Characters of permafrost. *J. Glaciol. Geocryol.* **2007**, *29*, 426–432. [CrossRef]
18. Mu, C.; Zhang, T.; Cao, B.; Wan, X.; Peng, X.; Cheng, G. Study of the organic carbon storage in the active layer of the permafrost over the Eboling Mountain in the upper reaches of the Heihe River in the Eastern Qilian Mountains. *J. Glaciol. Geocryol.* **2013**, *35*, 1–9.
19. Map of permafrost distribution in the Qilian Mountains. National Tibetan Plateau/Third Pole Environment Data Center. 2020. Available online: https://cstr.cn/18406.11.Geocry.tpdc.270456 (accessed on 16 August 2023).
20. Qi, J.; Ma, W. State-of-art of research on mechanical properties of frozen soils. *Rock Soil Mech.* **2010**, *31*, 133–143.
21. Usai, S. *A New Approach for Long Term Monitoring of Deformations by Differential SAR Interferometry*; Delft University of Tech: Delft, The Netherlands, 2001; pp. 1–165, ISBN 90-407-2189-0.
22. Berardino, P.; Fornaro, G.; Lanari, R.; Sansosti, E. A new algorithm for surface deformation monitoring based on small baseline differential SAR interferograms. *IEEE Trans. Geosci. Remote Sens.* **2002**, *40*, 2375–2383. [CrossRef]
23. Li, S.; Xu, W.; Li, Z. Review of the SBAS InSAR Time-series algorithms, applications, and challenges. *Geod. Geodyn.* **2022**, *13*, 114–126. [CrossRef]
24. Du, Q.; Li, G.; Chen, D.; Zhou, Y.; Qi, S.; Wu, G.; Chai, M.; Tang, L.; Jia, H.; Peng, W. SBAS-InSAR-Based analysis of surface deformation in the eastern tianshan mountains, China. *Front. Earth Sci.* **2021**, *9*, 729454. [CrossRef]

25. Hu, J.; Li, Z.; Zhu, J.; Liu, J. *Theory and Application of Monitoring 3-D Deformation with InSAR*; Science Press: Beijing, China, 2021.
26. Frauenfeld, O.W.; Zhang, T.; Mccreight, J.L. Northern hemisphere freezing/thawing index variations over the twentieth century. *Int. J. Climatol. A J. R. Meteorol. Soc.* **2007**, *27*, 47–63. [CrossRef]
27. Wu, T.; Wang, Q.; Zhao, L.; Batkhishig, O.; Watanabe, M. Observed trends in surface freezing/thawing index over the period 1987–2005 in Mongolia. *Cold Reg. Sci. Technol.* **2011**, *69*, 105–111. [CrossRef]
28. Luo, D.; Jin, H.; Jin, R.; Yang, X.; Lü, L. Spatiotemporal variations of climate warming in northern Northeast China as indicated by freezing and thawing indices. *Quat. Int.* **2014**, *349*, 187–195. [CrossRef]
29. Peng, X.; Zhang, T.; Cao, B.; Wang, Q.; Wang, K.; Shao, W.; Guo, H. Changes in freezing-thawing index and soil freeze depth over the Heihe River Basin, western China. *Arct. Antarct. Alp. Res.* **2016**, *48*, 161–176. [CrossRef]
30. Guglielmin, M. Ground surface temperature (GST), active layer and permafrost monitoring in continental Antarctica. *Permafr. Periglac. Process.* **2006**, *17*, 133–143. [CrossRef]
31. Fujun, N.; Guodong, C.; Yuanming, L.; Dewu, J. Instability study on thaw slumping in permafrost regions of Qinghai-Tibet Plateau. *Chin. J. Geotech. Eng.* **2004**, *26*, 402–406.
32. Orlowsky, B.; Seneviratne, S.I. Global changes in extreme events: Regional and seasonal dimension. *Clim. Chang.* **2012**, *110*, 669–696. [CrossRef]
33. Huggel, C.; Clague, J.J.; Korup, O. Is climate change responsible for changing landslide activity in high mountains? *Earth Surf. Process. Landf.* **2012**, *37*, 77–91. [CrossRef]
34. Owczarek, P.; Opała-Owczarek, M.; Boudreau, S.; Lajeunesse, P.; Stachnik, Ł. Re-activation of landslide in sub-Arctic areas due to extreme rainfall and discharge events (the mouth of the Great Whale River, Nunavik, Canada). *Sci. Total Environ.* **2020**, *744*, 140991. [CrossRef] [PubMed]
35. Chen, J.; Zhang, J.; Wu, T.; Hao, J.; Wu, X.; Ma, X.; Zhu, X.; Lou, P.; Zhang, L. Activity and Kinematics of Two Adjacent Freeze–Thaw-Related Landslides Revealed by Multisource Remote Sensing of Qilian Mountain. *Remote Sens.* **2022**, *14*, 5059. [CrossRef]
36. Patton, A.I.; Rathburn, S.L.; Capps, D.M. Landslide response to climate change in permafrost regions. *Geomorphology* **2019**, *340*, 116–128. [CrossRef]
37. Gariano, S.L.; Guzzetti, F. Landslides in a changing climate. *Earth-Sci. Rev.* **2016**, *162*, 227–252. [CrossRef]
38. Pavlova, I.; Jomelli, V.; Brunstein, D.; Grancher, D.; Martin, E.; Déqué, M. Debris flow activity related to recent climate conditions in the French Alps: A regional investigation. *Geomorphology* **2014**, *219*, 248–259. [CrossRef]
39. McRoberts, E.; Morgenstern, N.R. The stability of thawing slopes. *Can. Geotech. J.* **1974**, *11*, 447–469. [CrossRef]
40. Ding, Y.; Zhang, S.; Zhao, L.; Li, Z.; Kang, S. Global warming weakening the inherent stability of glaciers and permafrost. *Sci. Bull.* **2019**, *64*, 245–253. [CrossRef] [PubMed]
41. Lacelle, D.; Brooker, A.; Fraser, R.H.; Kokelj, S.V. Distribution and growth of thaw slumps in the Richardson Mountains–Peel Plateau region, northwestern Canada. *Geomorphology* **2015**, *235*, 40–51. [CrossRef]
42. Savi, S.; Comiti, F.; Strecker, M.R. Pronounced increase in slope instability linked to global warming: A case study from the eastern European Alps. *Earth Surf. Process. Landf.* **2021**, *46*, 1328–1347. [CrossRef]
43. Ma, L.-F.; Niu, F.-J.; Yang, N.-F. Analysis on ground temperature changes and landslide process of thaw slumping in permafrost regions. *Hydrogeol. Eng. Geol.* **2006**, *33*, 53–56.
44. Niuli, L.; Xuesong, M. Influence of humidity on per—Mafrostsubgradestabilityin Qinghai-Tibethighway. *Subgrade Eng.* **2011**, *23*, 5–11.
45. Jin, D.-W.; Sun, J.-F.; Fu, S.-L. Discussion on landslides hazard mechanism of two kinds of low angle slope in permafrost region of Qinghai-Tibet plateau. *Yantu Lixue (Rock Soil Mech.)* **2005**, *26*, 774–778.
46. Che, A.-l.; Wu, Z.-j.; Wang, P. Stability of pile foundations base on warming effects on the permafrost under earthquake motions. *Soils Found.* **2014**, *54*, 639–647. [CrossRef]
47. Moro, M.; Chini, M.; Saroli, M.; Atzori, S.; Stramondo, S.; Salvi, S. Analysis of large, seismically induced, gravitational deformations imaged by high-resolution COSMO-SkyMed synthetic aperture radar. *Geology* **2011**, *39*, 527–530. [CrossRef]
48. Bontemps, N.; Lacroix, P.; Doin, M.-P. Inversion of deformation fields time-series from optical images, and application to the long term kinematics of slow-moving landslides in Peru. *Remote Sens. Environ.* **2018**, *210*, 144–158. [CrossRef]